Med Biol Eng Comput (2017) 55:2001–2014
DOI 10.1007/s11517-017-1646-6

ORIGINAL ARTICLE

A tool for validating MRI-guided strategies: a digital breathing CT/MRI phantom of the abdominal site

Chiara Paganelli[1] · Paul Summers[2] · Chiara Gianoli[3,4] · Massimo Bellomi[2,5] · Guido Baroni[1,6] · Marco Riboldi[1]

Received: 12 June 2016 / Accepted: 25 March 2017 / Published online: 8 April 2017

Abstract Dynamic magnetic resonance imaging (MRI) is emerging as the elected image modality for organ motion quantification and management in image-guided radiotherapy. However, the lack of validation tools is an open issue for image guidance in the abdominal and thoracic organs affected by organ motion due to respiration. We therefore present an abdominal four-dimensional (4D) CT/MRI digital phantom, including the estimation of MR tissue parameters, simulation of dedicated abdominal MR sequences, modeling of radiofrequency coil response and noise, followed by k-space sampling and image reconstruction. The phantom allows the realistic simulation of images generated by MR pulse sequences with control of scan and tissue parameters, combined with co-registered CT images. In order to demonstrate the potential of the phantom in a clinical scenario, we describe the validation of a virtual T1-weighted 4D MRI strategy. Specifically, the motion extracted from a T2-weighted 4D MRI is used to warp a T1-weighted breath-hold acquisition, with the aim of overcoming trade-offs that limit T1-weighted acquisitions. Such an application shows the applicability of the digital CT/MRI phantom as a validation tool, which should be especially useful for cases unsuited to obtain real imaging data.

Keywords MRI guidance · Digital phantom · 4DMRI · Radiotherapy

✉ Chiara Paganelli
chiara.paganelli@polimi.it

[1] Dipartimento di Elettronica, Informazione e Bioingegneria, Politecnico di Milano, Milan, Italy

[2] Division of Radiology, Istituto Europeo di Oncologia, Milan, Italy

[3] Department of Experimental Physics-Medical Physics, Ludwig-Maximilians-Universität München (LMU Munich), Munich, Germany

[4] Department of Radiation Oncology, Ludwig-Maximilians-Universität München (LMU Munich), Munich, Germany

[5] Department of Oncology, Università degli Studi di Milano, Milan, Italy

[6] Bioengineering Unit, Centro Nazionale di Adroterapia Oncologica, Pavia, Italy

1 Introduction

Over the last few years, there has been growing interest in the use of magnetic resonance imaging (MRI) in image-guided radiotherapy. This is due to several intrinsic advantages of MRI with respect to computed tomography (CT), such as the absence of ionizing radiation, better soft tissue contrast and lower acquisition time in dynamic acquisition mode. Specifically, the concept of dynamic MRI has been used to evaluate organ motion due to respiration for both treatment planning and delivery in a number of works [7, 8, 12, 35, 36, 45, 49–51, 55] and is being brought to the fore by the emerging integration of MRI with treatment delivery units for a fully MRI-guided treatment [16, 24, 26, 32].

Four-dimensional (4D) MRI is typically achieved through the retrospective sorting of fast, dynamically acquired T2-weighted images [8, 35, 40, 41, 49], as these tend to allow a better contrast and spatiotemporal trade-off than dynamic T1-weighted acquisitions [41]. The availability of MR images with other weightings could, however, allow more appropriate description of tumors for specific functions (e.g., T1-weighted vs. T2-weighted images). Integrating the information from different imaging modalities has been widely reported in the literature as a means to extend the description of a tumor, as, for example, with

CT and MRI [9, 11, 28, 30], in order to provide complementary anatomical descriptions. Specifically to account for organ motion, Yu et al. [57] proposed the registration of 4D CT and gated MRI to integrate the motion information provided by the 4D CT with the well-contrasted anatomical information visible in MRI. Mapping the motion extracted from 4D MRI to a static 3D CT scan represents an alternative approach to generate patient-specific 4D CT data set [6, 56]. The tumor description can be further enriched with functional information (e.g., from positron emission tomography, PET) to provide tissue metabolic activity [38]. This is particularly important for localizing functional biomarkers in their anatomical context, as has been brought to prominence through the growing use of hybrid PET/CT and PET/MRI scanners [38, 44]. The need to compensate for organ motion in the abdomen is still a challenge in PET imaging, where the necessity of measuring adequate count statistics for image reconstruction necessitates data collection over a prolonged period and hence across numerous respiratory cycles. The use of 4D PET for the optimization of radiotherapy [10], as well as the application of dedicated motion correction strategies [5, 17, 27], is currently under investigation. Relevant to the multimodal description of tumors, Gianoli et al. [20] introduced the so-called virtual 4D PET strategy, entailing the application of a 4D CT motion model to free-breathing PET acquisitions to avoid the acquisition of time-resolved PET images.

However, the lack of tools for validation of algorithms and methods in image guidance remains an open issue, with particular reference to MRI when anatomical changes due to respiratory motion are involved. A standard approach to validation is the acquisition of in vivo images as ground truth [52], but these are not always available. Other solutions involve scanning MRI-compatible moving-structure phantoms [8, 54], which typically do not reflect the real internal anatomy. An MRI-compatible anthropomorphic moving phantom is under development [39], but the use of physical phantoms is generally limited due to their costs and inability to mimic the complexity of motion encountered in vivo.

Digital phantoms offer a practical approach to algorithm and method validation. Examples have already been proposed for CT with the 4D cardiac-torso (NCAT) phantom, which incorporates realistic beat-to-beat heart rate and respiratory motion variations and then the extended (XCAT) version [46]. A number of MRI simulators based on the Bloch equations have been developed, mainly for application to brain imaging [3, 29], where organ motion is generally neglected. The first implementations of digital MRI phantoms to incorporate motion for radiotherapy purposes were based on the 4D NCAT (and its extended XCAT version) by assigning MR properties to each tissue. Sharif et al. [48] proposed a physiologically improved NCAT phantom (PINCAT) in which the MR signal intensities were modified to validate a dynamic MR imaging scheme in real-time cardiac MRI applications. In Aja-Fernandez et al. [1], a digital moving phantom was generated by segmenting cardiac images from an in vivo acquisition and using random affine transformations to simulate motion. However, in these cases a gray level was assigned to each tissue, i.e., neglecting specific tissue properties and thus the impact of imaging parameters on image contrast and appearance. Wissmann et al. [53] designed a more realistic numerical phantom for cardiovascular MRI (MRXCAT) by extending the 4D XCAT phantom to MRI through the use of different tissues, MR signal models, multiple receiver coils and noise and finally selecting arbitrary trajectories and undersampled acquisition of the k-space for accelerated cine and myocardial perfusion imaging in specific cardiac MRI sequences.

In this work, we present the implementation of a 4D CT/MRI phantom based on 4D XCAT, with an approach similar to that proposed by Wissmann et al. [53], but extending the phantom to account for abdominal organ motion due to respiration. Subsequently, the phantom is used as validation tool for the virtual 4D imaging concept as applied to T1-weighted images in order to overcome the spatiotemporal limits of T1-weighted 4D MRI, in a fashion similar to that proposed in Gianoli et al. [20]. Finally, the virtual T1-weighted 4D MRI based on T2-weighted 4D images and a T1-weighted breath-hold acquisition is presented for five healthy volunteers.

2 Materials and methods

2.1 Dataset

For the derivation of a 4D CT/MRI Breathing Anthropomorphic Thorax (CoMBAT) phantom, a 4D CT XCAT [46] phantom of the abdomen was generated with 10 respiratory bins and a maximum motion of 15 mm in the superior–inferior (SI) direction (matrix: 256 × 256 × 200 voxels with 1 × 1 × 1 mm spacing).

To derive specific MR tissue parameters, dedicated MRI sequences were acquired with a 1.5-T scanner (Avanto, Siemens Medical Systems, Erlangen, Germany) to estimate relaxation parameters (T1 and T2) and proton density (ρ) values, in order to provide a more realistic simulation of abdominal tissues. Driven equilibrium single-pulse observation of T1 (DESPOT1, 11 flip angles in the range of 3°–45°) and T2 (DESPOT2, 8 flip angles in the range of 8°–64°) data were acquired on the abdomen of four healthy volunteers, and T1, T2 and ρ maps calculated as described in Deoni et al. [13, 14]. (TR/TE (repetition time/echo time): 3.5 ms/1.6 ms; matrix of 192 × 144 pixels

with 2.08 × 2.08 × 5 mm spacing for both DESPOT1 and DESPOT2).

In addition, three pulse sequences typically performed during abdominal imaging were of interest for this study to simulate MR sequences and perform the virtual 4D strategy. Specifically, T1- and T2-weighted acquisitions MRI series of the liver were acquired in four healthy volunteers, with parameters as follows:

- T1-weighted spoiled gradient echo sequence (volumetric interpolated breath-hold examination: VIBE) [43] acquired as an axial 3D image in breath-hold at inhalation (indicated as *T1_bh* in the following): TR/TE: 4.8 ms/1.75 ms; α (flip angle): 10°; bandwidth: 252 Hz per pixel; scan matrix: 240 × 320 pixels with spacing of 1.25 × 1.25 mm; slice thickness of 4 mm; percentage sampling of the k-space: 70% (along two phase encoding (PE) directions).
- T2-weighted balanced steady-state free precession sequence (TrueFISP) [18] used during free breathing to rapidly acquire dynamic oblique sagittal 2D images during respiratory motion: TR/TE: 2.6 ms/1.2 ms; α: 68°; bandwidth: 601 Hz per pixel; scan matrix: 256 × 224 pixels with spacing of 1.28 × 1.28 mm; slice thickness of 5 mm; acquisition time: 180 ms/slice with 20 slices × 20 frames. K-space percentage sampling: 65% (PE direction); acceleration factor: 2 with a generalized auto-calibrating partially parallel acquisition (GRAPPA) [21] using 16 auto-calibration (AC) lines.
- T1-weighted fast low-angle shot (FLASH) sequence [22] during free breathing, acquired as for TrueFISP: TR/TE: 5.6 ms/1.9 ms; α: 8°; bandwidth: 299 Hz per pixel; scan matrix: 144 × 192 pixels with spacing of 1.87 × 1.87 mm; slice thickness of 6 mm; acquisition time: 350 ms/slice with 20 slices × 30 frames; k-space sampling: 65% (PE direction); acceleration factor (GRAPPA) 2 using 16 AC lines.

The FLASH and TrueFISP sequences were optimized in order to provide adequate depiction of internal structures with sufficient temporal resolution to account for respiratory motion. In addition, the image-based 4D MRI approach proposed in Paganelli et al. [35] was applied to retrospectively sort the multiple sequences of both T1-weighted (FLASH) and T2-weighted (TrueFISP) MRI in 8 bins (i.e., to obtain *4DT1_flash* and *4DT2* MRI datasets, respectively).

The different acquisitions used in this work and their specific role in implementation and testing activities are summarized in Table 1.

2.2 CT/MRI breathing XCAT phantom (CoMBAT)

As proposed by Wissmann et al. [53], the phantom $P\left(\vec{k},t\right)$ is described in k-space through a combination of several weighting functions and transformation:

$$P\left(\vec{k},t\right) = R \cdot F \cdot \left[S(N_{\text{coil}}) \cdot T(T1,T2,\rho) \cdot C(\text{TE},\text{TR},\alpha) \cdot O(\vec{x},t) + n(\vec{x},t)\right]$$

Table 1 A summary of the datasets used in this study (see the following sections for details)

Dataset	Image modality	Dimensionality	Role
XCAT	Cardiac-torso CT phantom	4D	To build the 4D CT/MRI phantom (CoMBAT)
DESPOT sequences (DESPOT1 and DESPOT2)	MRI T1-weighted and T2-weighted Acquired on volunteers	3D breath-hold (axial)	To derive MRI tissue parameters (T1, T2 and proton density ρ) for the CoMBAT phantom
VIBE sequence	MRI T1-weighted Acquired on volunteers (breath-hold *T1_bh*) and simulated on the CoMBAT phantom for different respiratory phases (*4DT1*)	3D breath-hold (axial)	To serve as the volume to warp (*T1_bh*) for the virtual T1-weighted 4D MRI (*virtual_4DT1*)
TrueFISP sequence	MRI T2-weighted Acquired on volunteers and retrospectively sorted to obtain a T2-weighted 4D MRI (*4DT2*). Simulated on the CoMBAT phantom for different respiratory phases (*4DT2*)	Multislice 2D free-breathing (sagittal)	To derive the motion fields to apply to the *T1_bh* volume in creating *virtual_4DT1*
FLASH sequence	MRI T1-weighted Acquired on volunteers and retrospectively sorted to obtain a T1-weighted 4D MRI (*4DT1_flash*)	Multislice 2D free-breathing (sagittal)	To show trade-off limits.

where $O(\vec{x},t)$ represents the 4D XCAT phantom defined in space and time and $n(\vec{x},t)$ is the noise model. T is the tissue contribution as a function of relaxation times T1 and T2 and proton density ρ. The MR sequence is described by the operator C, which expresses the acquired signal as a function of TR, TE and α. S describes the sensitivity of N_{coil} coils. These physical space functions undergo Fourier transformation F, and the sampling of k-space R is applied to produce the raw k-space phantom $P\left(\vec{k},t\right)$. Once a complete k-space representation has been obtained, image reconstruction of the phantom can then follow via inverse Fourier transformation, as in in vivo image acquisition. Figure 1 shows the workflow of the CoMBAT implementation.

2.3 Tissue parameters T and MR sequences C

The VIBE and TrueFISP sequences were simulated for the generation of the CoMBAT phantom. At steady state, the signal equations C of the two sequences in terms of tissue-specific T1, T2 and ρ values and acquisition parameters TR, TE and flip angle (α) were as follows:

- VIBE: $C = \dfrac{\rho \sin\alpha\left(1-e^{-\frac{TR}{T1}}\right)}{\left(1-\cos\alpha e^{-\frac{TR}{T1}}\right)} e^{-\frac{TE}{T2}}$
- TrueFISP:

$$C = \rho \sin\alpha \frac{1-e^{-\frac{TR}{T1}}}{1-\left(e^{-\frac{TR}{T1}}-e^{-\frac{TE}{T2}}\right)\cos\alpha - e^{-\frac{TR}{T1}}e^{-\frac{TE}{T2}}} e^{-\frac{TE}{T2}}$$

The imaging parameters of the acquired in vivo VIBE and T2-weighted TrueFISP (TR, TE and α) were used in the sequence equations for the generation of the CoMBAT phantom.

The dominant properties determining tissue appearance in MR imaging are T1 and T2 relaxation times and the proton density of the tissue. Whereas relaxation times T1 and T2 were well defined in different works [4, 15], proton density values ρ were not available in the literature for all abdominal organs for 1.5-T scanners [33]. As reported in Sect. 2.1, specific DESPOT1 and DESPOT2 acquisitions were used to derive T1, T2 and the needed ρ-maps [13], from which values were obtained after segmentation of the organs present in the XCAT phantom. Unlike Wissmann

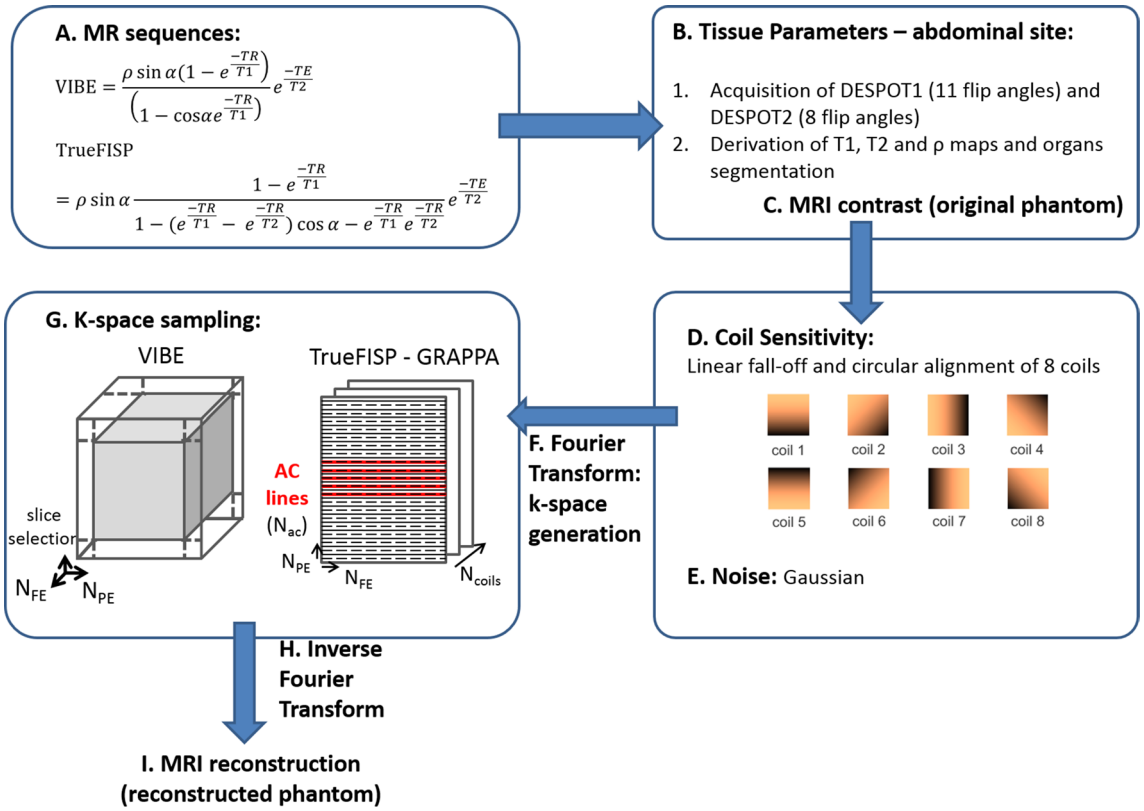

Fig. 1 CoMBAT workflow. (*A*) Simulation of two abdominal sequences (VIBE and TrueFISP). (*B*) Derivation of tissue parameters via DESPOT acquisitions to derive MRI contrast volumes (*C*). (*D*) Generation of a coil sensitivity map and (*E*) noise simulation. After the generation of the k-space through a Fourier transform (*F*) the k-space is sampled according to the specific MR sequence (partial volumetric sampling for VIBE and 2D GRAPPA sampling with auto-calibration (AC) lines for TrueFISP). (*H*) Inverse Fourier transform to derive the reconstructed MRI (*I*)

et al. [53], no contrast agent concentration was considered. Finally, the derived values (median among the four volunteers) were attributed to the corresponding tissue types in the XCAT phantom geometry.

2.4 Coil operator S and noise n

The effect of the coil sensitivity S was implemented as proposed in [33], in which the phantom MR signal $T(T1, T2, \rho) \cdot C(\mathrm{TE}, \mathrm{TR}, \alpha) \cdot O(\vec{x}, t)$ was combined with a simulated sensitivity map of the coil. The sensitivity maps had the form of a linear fall-off from the individual coils that were placed at uniformly on a circle around the abdomen ($N_{\mathrm{coils}} = 8$).

The presence of noise in MRI images was simulated by adding a Gaussian noise in order to match the signal-to-noise ratio of in vivo acquisitions (SNR = 20, computed on liver).

2.5 k-space generation F and k-space sampling R

The image-domain model was transformed to the k-space domain via a 3D discrete Fourier transform. Then, the k-space was sampled according to the sequence sampling approach. Specifically, the central 70% of k-space in the phase encoding directions was sampled for VIBE. The remainder of k-space was filled with zeros to provide smaller voxel size while keeping short imaging time. For TrueFISP, 65% of k-space was sampled based on the GRAPPA scheme [21], with the aim to speed up the MRI pulse sequence in order to acquire slices quickly, thus enabling the description of the respiratory cycle (i.e., acquisition time ranged from 180 to 300 ms, as proposed in the literature [40, 41]). In the GRAPPA algorithm, k-space is undersampled in the phase encoding direction (i.e., sampling factor = 2, acquisition of interleaved lines) and the missing k-space lines are synthesized by a linear combination of acquired neighboring k-space data using spatial information contained in the coil elements. The acquisition of additional lines in the k-space center is a form of self-calibration (i.e., AC = 16).

2.6 Image reconstruction and analysis

Once all k-space (3D for VIBE and 2D for TrueFISP) samples were obtained for a particular coil, an inverse Fourier transform was used to generate the uncombined image for that coil. The full set of N_{coils} images was then be combined using a normal sum of squares reconstruction [21].

Reconstructed images were qualitatively compared to in vivo T1-weighted (VIBE) and T2-weighted (TrueFISP) acquisitions, among visible well-contrasted anatomical structures. The reconstruction error matrixes were quantified by computing the difference between the original phantom and the reconstructed images, normalized with respect to the mean MR signal intensity. The normalized correlation between the original and the reconstructed images was also computed.

To analyze the reconstruction effects on the 4D motion, we also performed a deformable image registration (DIR) (www.plastimatch.org) [47] between exhale and inhale for both the original phantom and the reconstructed phantom. A Wilcoxon test ($\alpha = 5\%$) between the motions derived from the original and the reconstructed phantom was performed with both TrueFISP and VIBE sequences.

2.7 Virtual T1-weighted 4D MRI

T2-weighted (as well as T1-weighted) 4D MR images were derived from multislice free-breathing acquisitions and through the image-based retrospective sorting method proposed in Paganelli et al. [35] in four healthy volunteers. The virtual 4D imaging method involves the application of the motion field derived from the T2-weighted 4D MRI (i.e., *4DT2*) to the T1-weighted breath-hold acquisition (i.e., *T1_bh*) (Fig. 2). We first performed a rigid registration of the axial breath-hold acquisition at the inhale phase on the sagittal T2-weighted acquisition of the correspondent phase. The inhale phase in the *4DT2* was selected as the phase with the lowest diaphragm position [42]. Then, we performed a DIR (www.plastimatch.org) [47] between the inhale phase of the *4DT2* and each respiratory phase, by keeping the current phase as fixed and the inhale phase as moving image. The derived motion fields of all the respiratory phases were then used to warp the *T1_bh* acquisition in order to obtain a virtual T1-weighted 4D MRI (*virtual_4DT1*) for the volunteer data.

2.8 Validation of the virtual T1-weighted 4D MRI with CoMBAT

A *virtual_4DT1* was generated as described above for each volunteer, to overcome the limitations of 4DT1-weighted MR scanning (*4DT1_flash*) on soft tissue contrast and temporal resolution. Due to the absence of a ground truth (i.e., a 4DT1 acquired with VIBE for the different respiratory phases), we rely on the proposed 4D CoMBAT phantom in order to validate the *virtual_4DT1* strategy. As for volunteers, we simulated the same strategy by performing DIR of the current respiratory phase and the inhale phase of the *4DT2* phantom (i.e., via TrueFISP sequence simulation) and by applying the obtained motion fields to the inhale phase of the T1-weighted simulation (i.e., VIBE sequence), thus obtaining the missing respiratory phases. Finally, we compared the phases of the obtained *virtual_4DT1* with the ones provided by the simulated phantom with VIBE. This

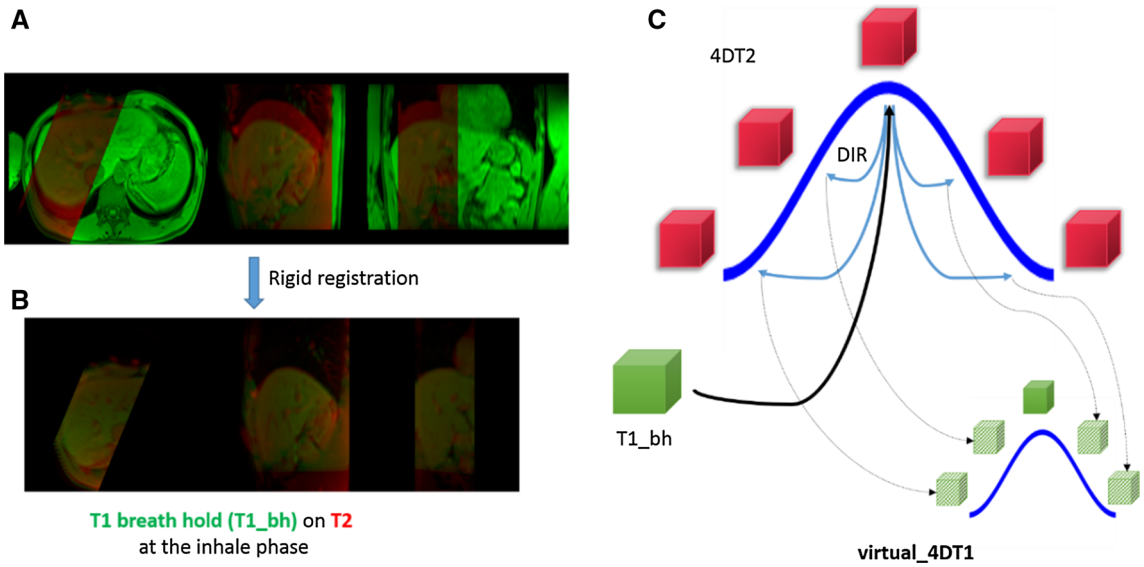

Fig. 2 Workflow of the virtual 4D imaging method. Overlap between the axial breath-hold T1-weighted acquisition (T1_bh in *green*) at the inhale phase with the correspondent respiratory phase of the T2-weighted 4D MRI (in *red*): **a** before and **b** after rigid registration. **c** Generation of the *virtual_4DT1* (*light green boxes*) by the application (*gray lines*) of the motion field obtained via DIR between *4DT2* phases (*light blue lines*) to the *T1_bh* (*dark green box*) obtained by rigid registration (*black line*) depicted in (**a**) and (**b**) (color figure online)

analysis relied on the use of automatically extracted landmarks [34] and in computing the error as 3D residual distance between landmarks of the *virtual_4DT1* phases and the correspondent ones in the 4D T1-weighted simulation with VIBE of the phantom (i.e., *4DT1*). The registration error derived from the DIR was also computed as 3D residual distance between identified landmarks of the registered phase on the inhale phase and the inhale phase, for both *4DT1* and *4DT2*.

2.9 Additional analysis

We further demonstrated the application of the 4D CoMBAT phantom through its use in a comparison of the capabilities of 4D T2-weighted and 4D T1-weighted imaging to describe an average respiratory cycle according to the image acquisition time. For this purpose, we considered a synthetic breathing signal generated with a cosine function $\cos(\omega t)^6$ to better mimic the end-expiration plateau [19]. The sampling of this signal was simulated according to the specific image acquisition time (i.e., 180 ms for TrueFISP and 350 ms for FLASH). We then binned the respiratory signal (100 s) in 8 bins to obtain an average respiratory cycle. Qualitative and quantitative analyses were performed based on soft tissue contrast to detect breathing motion.

3 Results

3.1 4D CoMBAT phantom

Table 2 compares the T1, T2 and ρ values reported in the literature with those derived via our DESPOT acquisitions. Background and air ρ were set to 0. Blood was not measured via DESPOT because flow effects were not compensated with the acquisition used; therefore, we applied the T1 and T2 values from the literature and the specific ρ value via in vivo T1- and T2-weighted acquisitions (1397 and 12,766, respectively). Across tissues, T1 and T2 values derived from DESPOT differed on average from the literature [4, 15] by 19 and 2%, respectively, and were not significantly different (Friedman test, $\alpha = 5\%$ for T1 and T2). Values for ρ obtained with DESPOT were higher than the few literature values available, amounting to almost 30% for spleen [33].

A visual comparison of T1- and T2-weighted images generated with the proposed phantom, and images acquired in vivo are given in Fig. 3, showing also a comparison with the CT phantom. The reconstruction error matrixes obtained computing the difference between the original phantom and the reconstructed one for all the respiratory phases were calculated (see Fig. 4 for peak inhalation and exhalation). The error matrixes showed pronounced edge

Table 2 Tissue parameters reported in the literature (left) and for the volunteers (right; mean ± S.D.) obtained from DESPOT maps

	Literature			DESPOT		
	T1 [ms]	T2 [ms]	ρ [a.u.]	T1 [ms]	T2 [ms]	ρ [a.u.]
Background	0	0	0	0	0	0
Air lung	0	0	0	0	0	0
Body	240[a]	85[a]	–	376 ± 10	70 ± 9	1336 ± 514
Bowel	–	–	–	122 ± 31	8 ± 4	117 ± 57
Muscle	900[a]	50[a]	–	825 ± 125	30 ± 5	3195 ± 721
Kidney cortex	652[b]	58[b]	–	921 ± 143	80 ± 16	1972 ± 337
Heart	870[a]	57[a]	–	1032 ± 103	49 ± 12	1346 ± 173
Liver	490[a]	40[a]	2182[c]	506 ± 57	36 ± 5	2023 ± 182
Blood	1200[a]	50[a]	–	–	–	–
Spleen	915[c]	80[c]	2088[c]	1466 ± 98	71 ± 15	1428 ± 96
Bone	732[b]	106[b]	1343[c]	753 ± 83	96 ± 8	1041 ± 149

Missing values are shown with –

[a] Bernstein et al. [4] (1.5 T), [b] Elmaoğlu and Çelik [15] (1.5 T), [c] Nyman et al. [33] (0.35 T)

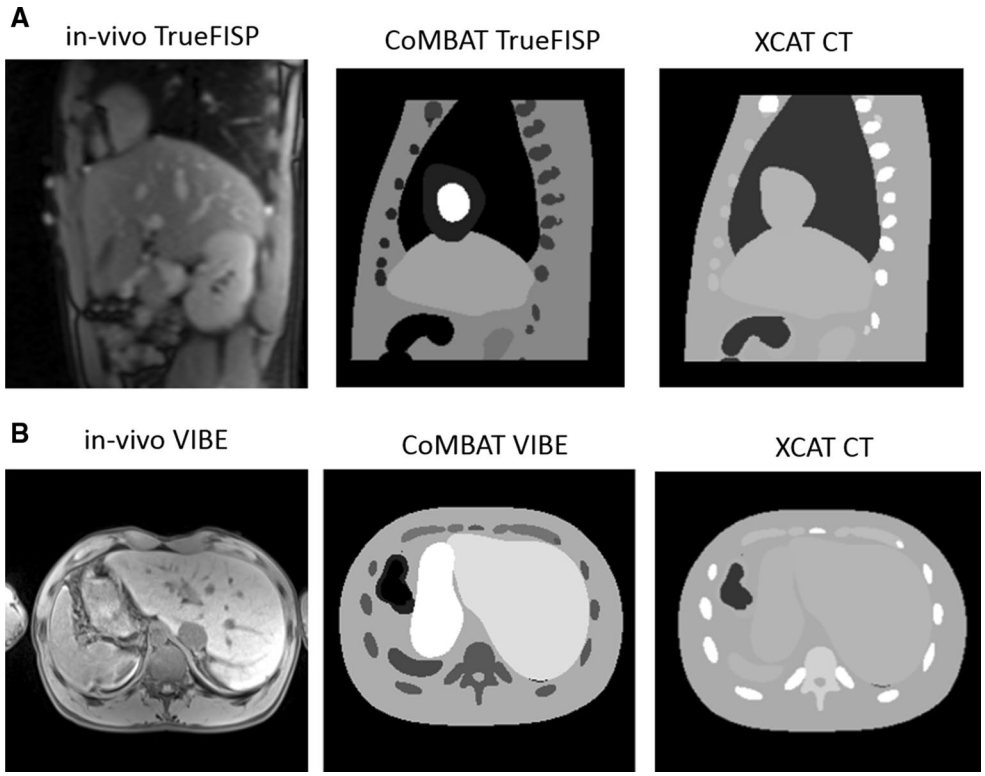

Fig. 3 In vivo acquisitions versus CoMBAT phantom for both TrueFISP (**a**) and VIBE (**b**), with the relevant CT of the XCAT phantom

effects for VIBE, whereas a more homogeneous distribution was seen for TrueFISP. The mean across all phases of the error matrixes were 15 and 9% for VIBE and TrueFISP, respectively. The normalized correlation coefficients were 0.89 and 0.98 for VIBE and TrueFISP, respectively.

An analysis of the effect of the reconstruction process on motion estimation was also performed by computing the motion fields between the exhale and inhale phases for the original and reconstructed phantoms. The difference (Wilcoxon, $\alpha = 5\%$) between these motion estimates

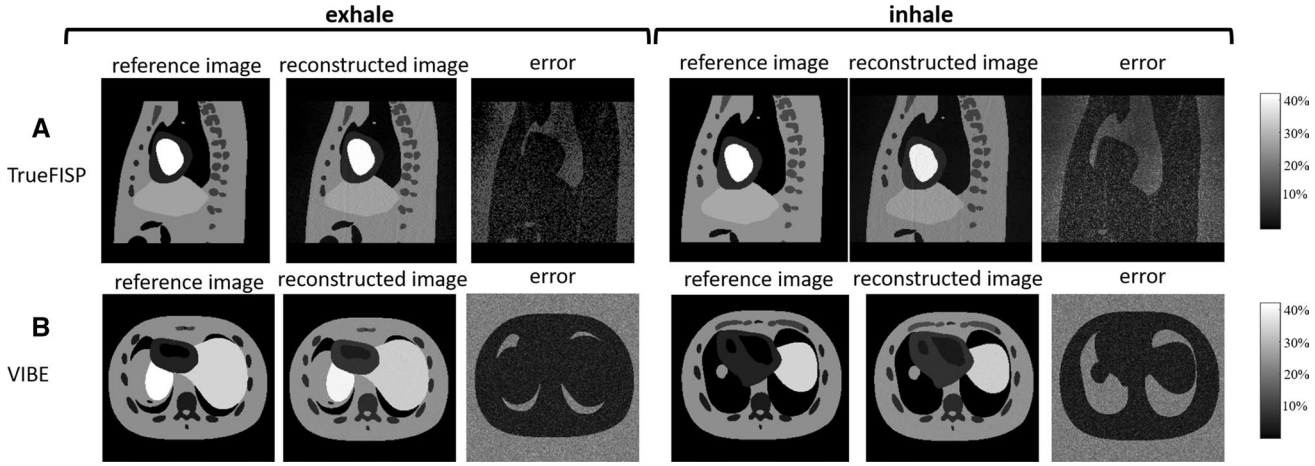

Fig. 4 Image reconstruction. **a** TrueFISP and **b** VIBE with the original MRI phantom, the reconstructed image and the error (%) for both exhale and inhale

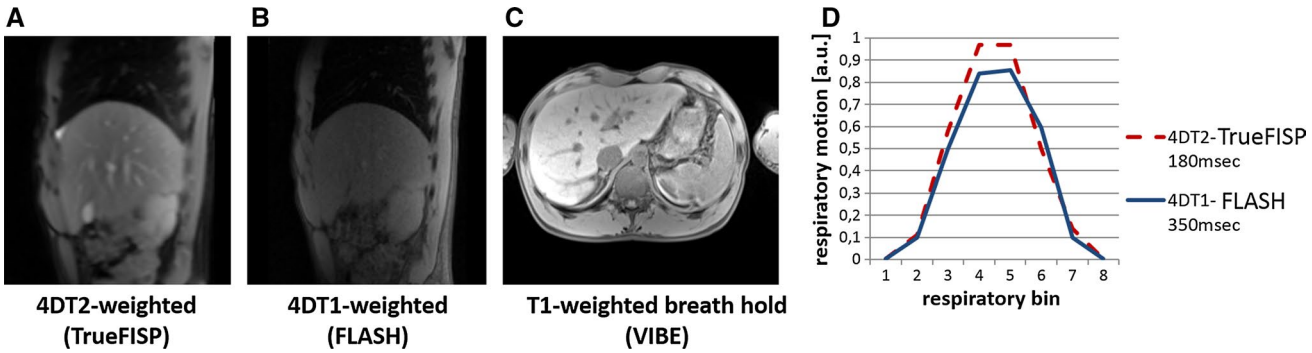

Fig. 5 In vivo T1- and T2-weighted acquisitions. **a** Sagittal *4DT2* acquired with TrueFISP, **b** sagittal *4DT1* acquired with FLASH, **c** axial *T1_bh* acquired with VIBE, **d** respiratory motion derived from *4DT1_flash* (*straight blue line*) and *4DT2* (*red dashed line*) sorting on a synthetic respiratory signal (color figure online)

was not significant for both the TrueFISP (5.96 ± 4.99 vs. 5.92 ± 4.92 mm for original vs. reconstructed) and the VIBE sequence (6.48 ± 4.64 vs. 6.08 ± 4.81 mm for original vs. reconstructed), with a mean difference of motion below the voxel size (i.e., 0.17 ± 0.22 mm for TrueFISP and 0.54 ± 0.45 mm for VIBE).

3.2 Virtual T1-weighted 4D MRI

The re-sorted free-breathing multislice T1-weighted 4D MRI, T2-weighted 4D MRI at the exhale phase and the T1-weighted volumetric breath-hold acquisition are illustrated in Fig. 5. Vessels and internal structures are visible in the *4DT2* acquisition and in *T1_bh*, but are very poorly represented in the *4DT1_flash*. The average respiratory motion derived by sorting the samples on a synthetic respiratory signal with the image acquisition time of the *4DT1_flash* (i.e., 350 ms) was lower than that of the *4DT2* acquisition, which had a lower image acquisition time (i.e., 180 ms).

Figure 6 shows the *virtual_4DT1* at the exhale phase for a representative volunteer. The derived *virtual_4DT1* at the exhale phase compensated for the motion derived from the *4DT2*. Both diaphragm and vessels resulted closer to the *4DT2* at the exhale phase. No comparison was made with the 4D T1-weighted derived with FLASH, due to its limited contrast in the definition of internal structures.

3.3 Validation via CoMBAT phantom

In order to validate the proposed approach, we rely on the 4D CoMBAT phantom generated for both TrueFISP and VIBE, thus creating a *virtual_4DT1* from the motion obtained between different respiratory phases of the *4DT2* derived with TrueFISP. The *virtual_4DT1* was then compared with the *4DT1* of the phantom obtained with the VIBE sequence.

Across all the respiratory phases, the registration error computed by the automatically extracted landmarks

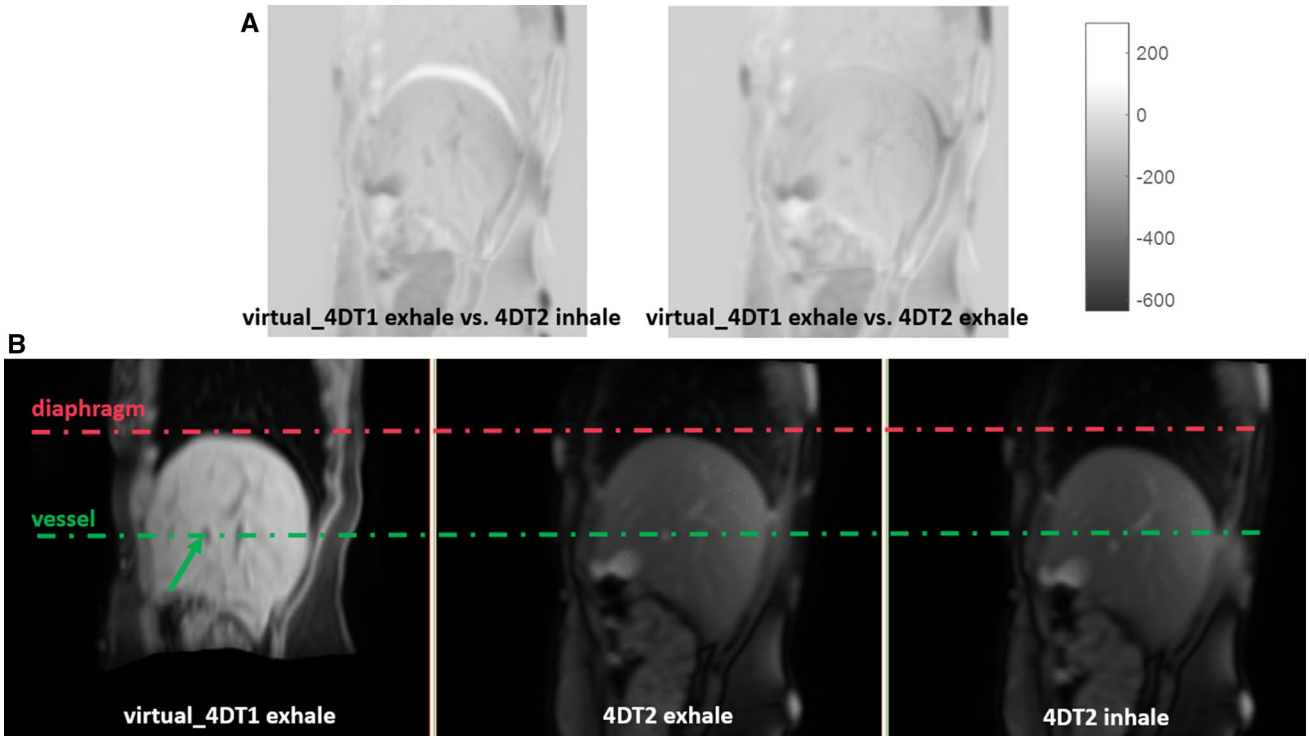

Fig. 6 *Virtual_4DT1* at the exhale phase for v03. **a** Differences in signal intensity between *virtual_4DT1* at the exhale phase and *4DT2* at the inhale phase and at the exhale phase. **b** *virtual_4DT1* at the exhale phase, *4DT2* at the exhale and inhale phase in sagittal view. The respiratory levels of the diaphragm and of a vessel are highlighted with *dashed lines*

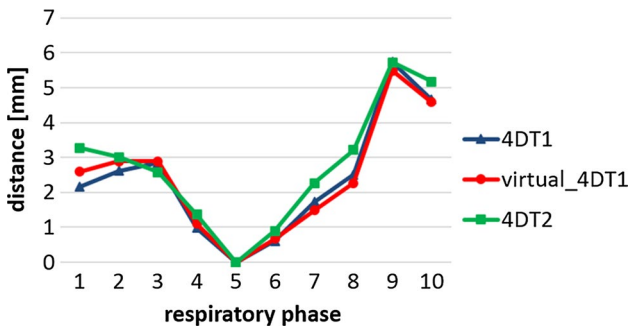

Fig. 7 Error of *virtual_4DT1* (*red circle*) and registration errors of *4DT1* (*blue triangle*) and *4DT2* (*green square*), derived from automatically extracted landmarks [34] (color figure online)

[34] was in mean 2.38 ± 1.76 and 2.75 ± 1.77 mm for *4DT1* and *4DT2*, respectively. A similar error was found between the generated *virtual_4DT1* and the *4DT1* of the phantom (2.40 ± 1.70 mm). A Wilcoxon test ($\alpha = 5\%$) did not show a significant difference between the three populations. Figure 7 depicts the registration errors for *4DT1* and *4DT2* and the error in deriving the *virtual_4DT1* for all the respiratory phases. Figure 8 shows the results of the estimated *virtual_4DT1* with respect to the *4DT1* at exhale and inhale phases.

4 Discussion

4.1 4D CoMBAT phantom

In this work, we described the implementation of an abdominal CT/MRI phantom by extending the 4D XCAT phantom designed by Segars et al. [46]. A similar work has previously been reported by Wissmann et al. [53] for cardiac acquisitions. Our aim was to provide a phantom able to describe respiratory motion of abdominal organs in MRI that can be used for the validation of MRI-guided techniques.

Proton density values for abdominal organs appear to be largely absent from the literature, and therefore, we derived them from ρ-maps obtained via DESPOT acquisitions. The tissue parameters T1 and T2 obtained in healthy volunteers were consistent with the literature [4, 15], lending confidence in the values obtained with DESPOT sequences. Even if this approach provides a realistic derivation of tissue parameters to include within the phantom simulation, limitations are present. Our acquisitions in fact did not, however, take into account inhomogeneities, which are known to influence DESPOT measurements [13]. Subtle corrections in the T1 and T2 values may therefore be warranted in the future. Bowel and heart

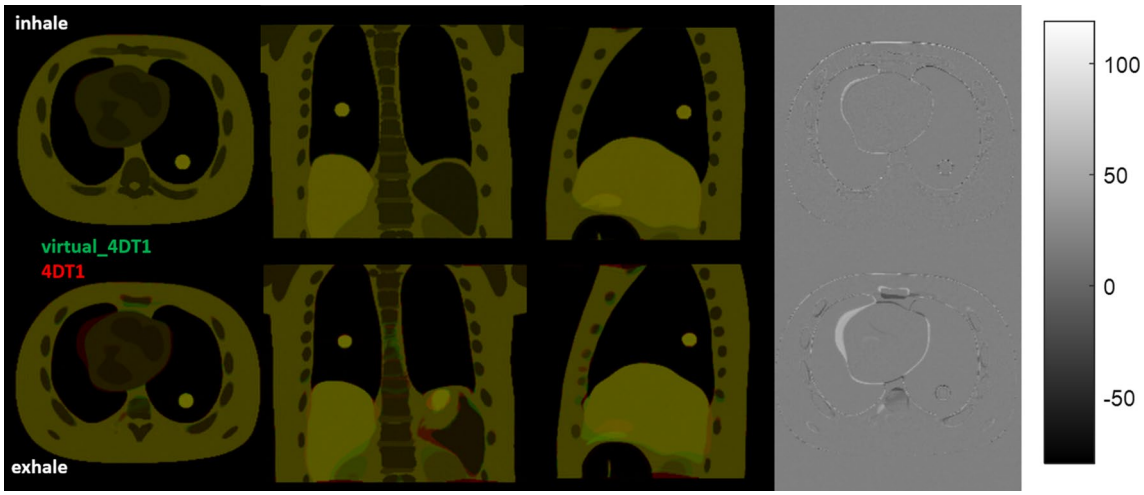

Fig. 8 *Virtual_4DT1* on phantom data. *First row* overlap of *virtual_4DT1* (*green*) and *4DT1* (*red*) at the inhale phase. *Second row* overlap of *virtual_4DT1* (*green*) and *4DT*1 (*red*) at the exhale phase. The difference of signal intensities in the axial view is reported in the fourth column. The inhale phase (*T1_bh*) is the respiratory phase to which the motion field is applied (color figure online)

were difficult to analyze due to artifacts associated with wall thickness (for bowel) and cardiac pulsation. Furthermore, we did not derive the values for blood due to flow effects [2] could not be adequately compensated for with the available DESPOT sequences.

Moreover, the signal equations of VIBE and TrueFISP do not include signal alterations due to motion during sampling [53], which have been shown to result in signal pile-up and mis-positioning [31]. In addition, spoiled gradient echo MRI, such as VIBE, is an MRI technique, which destroys residual transverse magnetization at the end of each excitation cycle. Conversely, steady-state free precession MRI as TrueFISP is a type of gradient echo MRI pulse sequence in which a steady, residual transverse magnetization is maintained between adjacent breathing cycles. Blood and other fluids may, however, exhibit spoiled contrast behavior, even though adjacent stationary tissue remains in a steady-state free precession. In order to reflect in vivo acquisitions, we therefore applied sequence-specific ρ values of blood, obtained via in vivo T1-weighted and T2-weighted acquisitions, allowing simulations to reproduce dark blood and bright blood in VIBE and TrueFISP, respectively, even if blood flow is not adequately accounted for by their signal equations. A compensation of such effects is possible through the incorporation of fluid dynamics simulations into the definition of the object model [23].

It should be also noted that the range of physical properties beyond ρ, T1 and T2 values that can influence MR signal intensity is quite large, including among others the velocity gradients (in liquids particularly), diffusion, magnetic susceptibility, temperature, chemical and magnetic exchange processes, as are the range of pulse sequences adapted to modify the relative weighting of these parameters. The coil sensitivity and noise used here are simplifications that could be adapted to reflect more realistic coil geometries and sensitivity profiles. All these factors therefore should be taken into account and added to the phantom simulation for a further improvement in tissue parameters definition and subsequent image contrast and appearance.

Nonetheless, the qualitative comparison with in vivo acquisitions (Fig. 3) showed the capability of the CoMBAT phantom to describe the MRI signal, allowing an increased image contrast with respect to CT. The reconstruction errors were 15 and 9% with a correlation of 0.89 and 0.99 for VIBE and TrueFISP, respectively, with more errors along the edges being present in the VIBE reconstruction (Fig. 3) due to a central sampling of the k-space and to a volumetric interpolation along two phase encoding directions in contrast to the calibrated and two-dimensional reconstruction of the TrueFISP acquisition. Background noise was present in both TrueFISP and VIBE reconstructions (i.e., more visible in TrueFISP due to the absence of errors along edges, as shown in Fig. 4). The motion estimated between the exhale and inhale phases was comparable in both the original and reconstructed phantoms for TrueFISP and VIBE, attesting that the reconstruction method does not affect the original motion.

We therefore proposed a 4D CT/MRI phantom, which can simulate MRI acquisitions while describing organ motion and provide a ground truth for the validation and testing of different MRI-guided strategies and MRI reconstruction methods. In addition, the MRI phantom combined with the corresponding CT images could represent an ideal framework to quantify the effects of MRI-based dosimetry, as proposed in recent studies [25, 37]. A further

improvement could be also the inclusion of the metabolic activity provided by the XCAT phantom in terms of PET simulation [46], thus providing a multimodal tool that can be used also in 4D PET/CT and PET/MRI imaging.

4.2 Virtual T1-weighted 4D MRI

Use of the CoMBAT phantom developed in this work was demonstrated in the validation of a *virtual_4DT1* strategy, which consisted in the application of the motion field derived from a T2-weighted 4D MRI (*4DT2*) to a 3D T1-weighted breath-hold image acquired in the peak inhalation phase (*T1_bh*). The aim was to estimate the missing respiratory phases and to overcome the limitations in obtaining a well-contrasted T1-weighted 4D MRI (*4DT1_flash*) with a temporal resolution able to describe a consistent average respiratory cycle.

The ability to achieve an optimal trade-off between spatial and temporal resolution and to acquire well-contrasted images is of primary importance in MRI-guided radiotherapy when organ motion is involved. The use of T2-weighted TrueFISP as fast sequence able to describe internal anatomy during respiration has been widely used in the literature [36, 40, 45, 50]. However, other MR sequences may allow better description of the tumor. We therefore proposed the acquisition of both multislice T2-weighted and T1-weighted images and their image-based retrospective sorting to create time-resolved volumes [35]. In optimizing the sequences for time and coverage, multislice acquisition was achieved with TrueFISP sequence in which internal structures were visible, conversely to FLASH sequence, in which a low contrast between organs was present. In addition, the retrospective sorting of T1-weighted slices led to an underestimation of the average respiratory motion, due to the higher image acquisition time than T2-weighted slices, as shown in the sampling of a synthetic respiratory signal.

As a means to overcome these limitations, a breath-hold volumetric T1-weighted at the peak inhalation phase with the VIBE sequence could be warped by applying the motion field derived from a higher temporal resolution *4DT2* MRI. An initial rigid registration is required between the *T1_bh* at the inhale phase and the corresponding phase within the *4DT2*. The rigid registration between *T1_bh* and the inhale phase of the *4DT2* showed errors below the maximum voxel size (i.e., 5 mm), as reported in previous works [28, 57]. Subsequent application of the motion field derived from *4DT2* to *T1_bh* to create a *virtual_4DT1* derived from patient data provided a visual impression of capturing organ motion. The absence of an acquired 4D T1-weighted MRI having the temporal resolution and the good contrast of the *4DT2* MRI, however, complicates the task of validating the derived *virtual_4DT1*.

As a surrogate approach to validation, we translated the proposed strategy onto the digital CoMBAT phantom, where we generated both *4DT1* (simulated with VIBE) and *4DT2* (simulated with TrueFISP). Also, we applied the motion field derived from the *4DT2* at inhale phase and the other *4DT2* respiratory phases to the peak inhalation phase image of the *4DT1*, in order to derive the other T1-weighted respiratory phases. These were then compared with the *4DT1* directly derived from the phantom. A mean error of 2.40 ± 1.70 mm was quantified among all respiratory phases in the *virtual_4DT1*, suggesting adequate performance of the method. Higher errors were observed for respiratory phases far from the inhale phase (Fig. 7). This was mainly due to the performance of the DIR algorithm: Errors in the DIR process were propagated in the *virtual_4DT1*. In fact, the errors quantified in the *virtual_4DT1* resulted in the same range of the *4DT1* and *4DT2* registration errors for all the respiratory phases.

We therefore propose a preliminary application of the CoMBAT phantom on a clinical scenario aiming at overcoming limitations in temporal 4DT1-weighted acquisitions, thus allowing a more appropriate description of tumor with different MRI weightings as well as organ motion in the clinical workflow. Future works will be focused on the use of the CoMBAT phantom for the validation of specific 4D resorting strategies such as navigator-based [51] and image-based [8, 35, 49, 55] methods as well as novel k-space resorting approaches [12], with the aim to provide benchmarks for the recent developments in 4D MRI.

5 Conclusion

We presented a digital abdominal 4D CT/MRI phantom (CoMBAT), which can be used as a framework for the validation of MR image reconstruction and quantitative post-processing approaches to improve organ motion quantification and compensation in radiotherapy. To illustrate the potential of the CoMBAT phantom, we described its application to a novel MRI-guided strategy able to overcome the limitations in contrast and temporal resolution of retrospective T1-weighted 4D MRI. Our proposal envisaged the acquisition of a volumetric breath-hold T1-weighted volumes and the application of the motion field derived from a faster, higher contrast T2-weighted 4D MRI, thus allowing the derivation of the missing respiratory phases to create a virtual T1-weighted 4D MRI (i.e., *virtual_4DT1*). The application of the method on the proposed CoMBAT phantom provided a validation of the strategy, which was not possible on real data, due to the absence of a proper T1-weighted 4D acquisition.

Future works should envision an improvement in the abdominal phantom for a better realistic simulation of in vivo acquisitions, such as the inclusion of vessels, spin history and additional effects such as susceptibility and enhancement due to contrast agents. Inclusion of compressed sensing and other techniques for accelerating image acquisition could be an additional further direction. Finally, the use of the proposed phantom for the validation of different 4D MRI-guided strategies will be exploited, as well as its application in multimodal imaging.

Acknowledgements This work was partially supported by AIRC, the Italian Association for Cancer Research. The author would also like to thank A. Pifferi for the help during tissue parameter estimation and G. Buizza and S. Cacciatore for the rigid registration assessment.

References

1. Aja-Fernandez S, Cordero-Grande L, Alberola-Lopez C. (2012) A MRI phantom for cardiac perfusion simulation. In: IEEE ISBI, pp 638–641
2. Axel L (1984) Blood flow effects in magnetic resonance imaging. AJR Am J Roentgenol 143(6):1157–1166
3. Benoit-Cattin H, Collewet G, Belaroussi B et al (2005) The SIMRI project: a versatile and interactive MRI simulator. J Magn Reson 173:97–115
4. Bernstein MA, Kevin FK, Xiaohong JZ (2004) Handbook of MRI pulse sequences. Elsevier Academic Press, p 961. ISBN:978-0-12-092861-3
5. Bettinardi V, Picchio M, Di Muzio N et al (2010) Detection and compensation of organ/lesion motion using 4D-PET/CT respiratory gated acquisition techniques. Radiother Oncol 96:311–316
6. Boye D, Lomax T, Knopf A (2013) Mapping motion from 4D-MRI to 3D-CT for use in 4D dose calculations: a technical feasibility study. Med Phys 40:061702
7. Brix L, Ringgaard S, Sørensen TS et al (2014) Three-dimensional liver motion tracking using real-time two-dimensional MRI. Med Phys 41:042302
8. Cai J, Chang Z, Wang Z et al (2011) Four-dimensional magnetic resonance imaging (4D-MRI) using image-based respiratory surrogate: a feasibility study. Med Phys 38:6384–6394
9. Carrillo A, Duerk JL, Lewin JS et al (2000) Semiautomatic 3-D image registration as applied to interventional MRI liver cancer treatment. IEEE Trans Med Imaging 19:175–185
10. Chirindel A, Adebahr S, Schuster D et al (2015) Impact of 4D-18FDG-PET/CT imaging on target volume delineation in SBRT patients with central versus peripheral lung tumors. Multireader comparative study. Radiother Oncol 115:335–341
11. Dean CJ, Sykes JR, Cooper RA et al (2012) An evaluation of four CT–MRI co-registration techniques for radiotherapy treatment planning of prone rectal cancer patients. Br J Radiol 85:61–68
12. Deng Z, Pang J, Yang W et al (2016) Four-dimensional MRI using three-dimensional radial sampling with respiratory self-gating to characterize temporal phase-resolved respiratory motion in the abdomen. Magn Reson Med 75:1574–1585
13. Deoni SC, Rutt BK, Peters TM (2003) Rapid combined T1 and T2 mapping using gradient recalled acquisition in the steady state. Magn Reson Med 49:515–526
14. Deoni SC, Kost JA, Adams PA et al (2004) Quantification of liver iron with rapid 3D R1 and R2 mapping with DESPOT1 and DESPOT2. Proc Int Soc Magn Reson Med 11:889
15. Elmaoğlu M, Çelik S (2012) MRI handbook: MR physics, patient, positioning, and protocols. Springer, Berlin
16. Fallone BG (2014) The rotating biplanar linac-magnetic resonance imaging system. Semin Radiat Oncol 24:200–202
17. Fayad H, Schmidt H, Wuerslin C et al (2015) Reconstruction-incorporated respiratory motion correction in clinical simultaneous PET/MR imaging for oncology applications. J Nucl Med 56:884–889
18. Fuchs F, Laub G, Othomo K (2003) TrueFISP - technical considerations and cardiovascular applications. Eur J Radiol 46:28–32
19. Gianoli C, Riboldi M, Spadea MF et al (2011) A multiple points method for 4D CT image sorting. Med Phys 38:656–667
20. Gianoli C, Riboldi M, Fontana G et al (2013) Optimized PET imaging for 4D treatment planning in radiotherapy: the virtual 4D PET strategy. Technol Cancer Res Treat 14(1):99–110
21. Griswold MA, Jakob PM, Heidemann RM et al (2002) Generalized autocalibrating partially parallel acquisitions (GRAPPA). Magn Reson Med 47:1202–1210
22. Haase A (1990) Snapshot flash MRI: applications to T1, T2, and chemical-shift imaging. Magn Reson Med 13:77–89
23. Jurczuk K, Kretowski M, Bellanger JJ et al (2013) Computational modeling of MR flow imaging by the lattice Boltzmann method and Bloch equation. Magn Reson Imaging 7:1163–1173
24. Keall P, Barton M, Crozier S (2014) The Australian magnetic resonance imaging-linac program. Semin Radiat Oncol 24:203–206
25. Kim J, Glide-Hurst C, Doemer A et al (2015) Implementation of a novel algorithm for generating synthetic CT images from magnetic resonance imaging data sets for prostate cancer radiation therapy. Int J Radiat Oncol Biol Phys 91:39–47
26. Lagendijk JJW, Raaymakers BW, van Vulpen M (2014) The magnetic resonance imaging-linac system. Semin Radiat Oncol 24:207–209
27. Lamare F, Fayad H, Fernandez P et al (2015) Local respiratory motion correction for PET/CT imaging: application to lung cancer. Med Phys 42:5903–5912
28. Lange T, Wenckebach TH, Lamecker H et al (2005) Registration of different phases of contrast-enhanced CT/MRI data for computer assisted liver surgery planning: evaluation of the state-of-the-art-methods. Int J Med Robot Comput Assist Surg 1:6–20
29. Liu F, Kijowski R, Block W (2014) Performance of multiple types of numerical MR simulation using MRiLab. Proc Int Soc Magn Reson, Med, p 5244
30. Maintz JBA, Viergever MA (1998) A survey of medical image registration. Med Image Anal 2:1–36
31. Moore JA, Steinman DA, Holdsworth DW et al (1999) Accuracy of computational hemodynamics in complex arterial geometries reconstructed from magnetic resonance imaging. Ann Biomed Eng 27:32–41
32. Mutic S, Dempsey JF (2014) The viewray system: magnetic resonance-guided and controlled radiotherapy. Semin Radiat Oncol 24:196–199
33. Nyman R, Ericsson A, Hemmingsson A et al (1986) T1, T2, and relative proton density at 0.35 T for spleen, liver, adipose tissue, and vertebral body: normal values. Magn Reson Med 3:901–910
34. Paganelli C, Peroni M, Riboldi M et al (2013) Scale invariant feature transform in adaptive radiation therapy: a tool for deformable image registration assessment and re-planning indication. Phys Med Biol 58:287–299

35. Paganelli C, Summers P, Bellomi M et al (2015) Liver 4DMRI: a retrospective image-based sorting method. Med Phys 8:4814–4821
36. Paganelli C, Seregni M, Fattori G et al (2015) Magnetic resonance imaging-guided versus surrogate-based motion tracking in liver radiation therapy: a prospective comparative study. Int J Radiat Oncol Biol Phys 91:840–848
37. Paradis E, Cao Y, Lawrence TS et al (2015) Assessing the dosimetric accuracy of magnetic resonance-generated synthetic CT images for focal brain VMAT radiation therapy. Int J Radiat Oncol Biol Phys 93:1154–1161
38. Parodi K (2015) Vision 20/20: positron emission tomography in radiation therapy planning, delivery, and monitoring. Med Phys 42:7153
39. Perrin R, Peroni M, Bernatowicz K (2014) A realistic breathing phantom of the thorax for testing new motion mitigation techniques with scanning proton therapy. Med Phys 41:111
40. Plathow C, Ley S, Fink C et al (2004) Analysis of intrathoracic tumor mobility during whole breathing cycle by dynamic MRI. Int J Radiat Oncol Biol Phys 59:952–959
41. Plathow C, Klopp M, Fink C et al (2005) Quantitative analysis of lung and tumour mobility: comparison of two time-resolved MRI sequences. Br J Radiol 78:836–840
42. Rit S, van Herk M, Zijp L et al (2012) Quantification of the variability of diaphragm motion and implications for treatment margin construction. Int J Radiat Oncol Biol Phys 82:399–407
43. Rofsky NM, Lee VS, Laub G et al (1999) Abdominal MR imaging with a volumetric interpolated breathhold examination. Radiology 212:876–884
44. Sauter AW, Schwenzer N, Divine MR et al (2015) Image-derived biomarkers and multimodal imaging strategies for lung cancer management. Eur J Nucl Med Mol Imaging 42:634–643
45. Sawant A, Keall P, Pauly KB et al (2014) Investigating the feasibility of rapid MRI for imageguided motion management in lung cancer radiotherapy. BioMed Res Int. doi:10.1155/2014/485067
46. Segars P, Sturgeon G, Mendonca S et al (2010) 4D XCAT phantom for multimodality imaging research. Med Phys 37:4902–4915
47. Shackleford J, Kandasamy N, Sharp GC (2010) On developing B-spline registration algorithms for multi-core processors. Phys Med Biol 55:6329–6351
48. Sharif B, Bresler Y (2014) Adaptive real-time cardiac MRI using PARADISE: validation by the physiologically improved NCAT phantom. Proc IEEE Int Symp Biomed Imaging. doi:10.1109/ISBI.2007.357028
49. Tryggestad E, Flammang A, Han-Oh S et al (2013) Respiration-based sorting of dynamic MRI to derive representative 4D-MRI for radiotherapy planning. Med Phys 40:051909
50. Tryggestad E, Flammang A, Hales R et al (2013) 4D tumor centroid tracking using orthogonal 2D dynamic MRI: implications for radiotherapy planning. Med Phys 40:091712
51. von Siebenthal M, Székely G, Gamper U et al (2007) 4D MR imaging of respiratory organ motion and its variability. Phys Med Biol 52:1547–1564
52. Weon C, Hyun Nam W, Lee D et al (2015) Position tracking of moving liver lesion based on real-time registration between 2D ultrasound and 3D preoperative images. Med Phys 42:335–345
53. Wissmann L, Santelli C, Segars P et al (2014) MRXCAT: realistic numerical phantoms for cardiovascular magnetic resonance. J Cardiovasc Magn Reson 16:63
54. Quasar. http://modusmed.com/qa-phantoms/mri-respiratory-motion
55. Yang J, Cai J, Wang H et al (2014) Four-dimensional magnetic resonance imaging using axial body area as respiratory surrogate: initial patient results. Int J Radiat Oncol Biol Phys 88:907–912
56. Yang YX, Teo SK, Van Reeth E et al (2015) A hybrid approach for fusing 4D-MRI temporal information with 3D-CT for the study of lung and lung tumor motion. Med Phys 48:4484–4496
57. Yu JI, Kim JS, Park HC et al (2013) Evaluation of anatomical landmark position differences between respiration-gated MRI and four-dimensional CT for radiation therapy in patients with hepatocellular carcinoma. Br J Radiol 86:1–7

Chiara Paganelli is a Post-Doc fellow at the Department of Electronic, Information and Bioengineering, Politecnico di Milano, Italy. Her research interests include MRI guidance in radiotherapy.

Paul Summers is a Research Scientist at the Istituto Europeo di Oncologia, Milano, Italy. He has a long experience in MRI acquisition and optimization.

Chiara Gianoli is a Post-Doc fellow at the Ludwig-Maximilians-Universität, München (LMU Munich), Germany. Her research is focused on PET image analysis and reconstruction.

Massimo Bellomi is the Director of the Department of Radiology at the Istituto Europeo di Oncologia, Milano, and his activity relies on advanced diagnostic imaging.

Guido Baroni is Associate Professor at Politecnico di Milano, Department of Electronic, Information and Bioengineering. His research interest comprises technologies for motion management.

Marco Riboldi is Assistant Professor at Politecnico di Milano, Department of Electronic, Information and Bioengineering. His research relies on technologies for time-resolved image-guided treatments.